Article:

Davies, CJ orcid.org/0000-0002-1074-3815 and Gubbins, D orcid.org/0000-0002-8125-4752 (2011) A buoyancy profile for the Earth′s core. Geophysical Journal International, 187 (2). pp. 549-563. ISSN 0956-540X

https://doi.org/10.1111/j.1365-246X.2011.05144.x submitted to *Geophys. J. Int.*

A buoyancy profile for the Earth's core

C. J. Davies[1,2] & D. Gubbins[1,2,3]

[1] *Scripps Institution of Oceanography, La Jolla, CA, 92092-0225, USA*

[2] *School of Earth & Environment, University of Leeds, Leeds LS2 9JT, UK*

[3] *Miller Institute, Department of Earth & Planetary Science, University of California Berkeley, CA 94720-4767, USA*

Key words: Geodynamo, Earth's Core

SUMMARY

We investigate the thermal and chemical buoyancy forces that drive convection in Earth's liquid outer core and derive a radial buoyancy profile that can be used in geodynamo models. We assume the core is well-mixed, adiabatic and cools as a result of mantle convection. The buoyancy profile is developed for a Boussinesq fluid and incorporates secular cooling, latent heat release at the inner core boundary, radiogenic heating, the effect of the adiabat, and compositional buoyancy due to inner core freezing. Surprisingly, these complex effects can be modelled accurately by a simple combination of bottom heating and near-uniform heat sinks, which is achieved using a cotemperature formulation that converts compositional effects into effective thermal effects. The relative importance of internal and bottom heating is then defined by just two parameters, the cooling rate at the core-mantle boundary (CMB) and the uniform rate of internal radiogenic heat production, both of which can be obtained from core evolution calculations. We vary these parameters in geodynamo models and compare basic features of the generated fields with the geomagnetic field; in this manner we link core evolution models, geodynamo simulations and geomagnetic observations.

We consider three end-member scenarios for core evolution: 1) rapid cooling and a young inner core; 2) moderate cooling and neutral stability at the CMB; 3) slow cooling and enough radiogenic heating to allow the inner core to be 3.5 Gyr old. We find that compositional buoyancy dominates thermal buoyancy everywhere except near the CMB, even with large amounts of radiogenic heating, and buoyancy forces are far larger at depth than higher up. Reducing the cooling rate and increasing radiogenic heating reduces the drop in the superadiabatic gradient between the inner and outer boundaries: for rapid cooling the drop is by a factor 50; for slow cooling it is a factor of 5. We demonstrate the effects of these different buoyancy profiles in numerical simulations as a function of the Rayleigh number. At low Rayleigh number the internal velocity and magnetic fields vary between the core evolution scenarios, but these differences do not affect the surface field. Significant differences in the surface field emerge when the Rayleigh number is sufficiently large. For rapid cooling we find dipolar magnetic fields in the time-average that reverse and are dominated by large-scale features at high latitudes. Moderate cooling results in magnetic fields that are always stable and dominantly dipolar. Slow cooling produces multipolar magnetic fields that reverse very frequently. This preliminary study suggests that the generated fields are sufficiently different that geodynamo simulations together with geomagnetic observations could be used to discriminate between different core evolution scenarios.

1 INTRODUCTION

The Earth's magnetic field is generated by dynamo action in the liquid iron core. The dynamo is driven by a combination of thermal and compositional (*thermochemical*) convection, which in turn draws its power from the Earth's continuing slow cooling. The detailed nature of the geodynamo and, in all probability, of the observed geomagnetic field depends on the *buoyancy profile* driving the convection, the radial variation of the buoyancy force entering the Navier-Stokes equation. Numerical models of convection-driven dynamos have shown that dynamo action can be achieved with a variety of simple buoyancy profiles, including purely internal heating (Grote et al., 1998; Willis et al., 2007; Hori et al., 2010), purely bottom heating (Christensen et al., 1999, 2001; Heimpel et al., 2005), combined internal and bottom heating (Busse et al., 2003) and internal cooling (Olson, 2007; Driscoll & Olson, 2009). Thermochemical convection has also been modelled, either by combining thermal and chemical buoyancy sources into a single buoyancy profile (Aubert et al., 2009; Driscoll & Olson, 2009; Olson et al., 2010) or by separately solving two diffusion equations (Glatzmaier & Roberts, 1996; Manglik et al., 2010).

Relatively little work has been done to directly compare the effects of different buoyancy profiles on the outputs of numerical dynamo models. For pure thermal or chemical buoyancy Kutzner & Christensen (2000) and Ogden et al. (2006) compared dynamos driven by bottom heating, internal heating, and internal cooling, Sreenivasan & Gubbins (2008) studied the effect of stratification on core-mantle interaction using combinations of internal and bottom heating and Rotvig (2009) and Kutzner & Christensen (2002) investigated how different heating modes affect polarity reversal characteristics. Even less is known about the comparative effects of different buoyancy sources in thermochemically driven dynamos, primarily because most current models describe the thermochemical buoyancy profile by dimensionless forcing parameters representing the buoyancy flux at the outer boundary and an internal source/sink term, thereby obviating the need to calculate individual contributions to the buoyancy profile (e.g. Aubert et al., 2009; Olson et al., 2010). This is surprising, partly because the buoyancy profile is one of the easier quantities to change and study within a geodynamo simulation, and partly because different buoyancy profiles come at essentially equal computational expense. While we cannot yet reach the high Rayleigh numbers likely to hold in the core, we can easily explore the effects of changing the type of heating and cooling. Furthermore, as we highlight in Section 4 of this paper, key outputs of the simulations (the very "character" of the dynamo model) are sensitive to the buoyancy profile. Considering the vast parameter space that geodynamo models must span, the production of a universal buoyancy profile is clearly important; this is the object of this paper. To achieve this goal we develop a set of equations that

(i) Express individual thermal and compositional contributions to the overall buoyancy profile;

(ii) Allow quantitative comparisons between thermal and compositional effects and between internal and basal effects;

(iii) Can be implemented in geodynamo calculations.

We seek to use the results of core evolution models as inputs into these equations and, ultimately, into geodynamo simulations. By comparing the dynamo behaviour for various buoyancy profiles we aim to distinguish between different radial buoyancy distributions and to interpret the results in the context of core evolution models.

Realistic buoyancy profiles are readily derivable from the many studies of core evolution, which use the equations of energy and entropy to model the slow evolution of Earth's outer core. Averaging these equations over some timescale that is long compared to characteristic timescales associated with the dynamo process but short compared to the evolutionary timescale averages out fluctuations associated with the convection, leaving equations that describe changes in the *reference state* of the core (Gubbins et al., 1979; Braginsky & Roberts, 1995; Jones, 2007). To define the reference state we suppose the core to cool as a result of mantle convection, which fixes the heat-flux from the outer core and imposes a cooling rate dT_o/dt on the core-mantle boundary (CMB). We also suppose the core to be of near-uniform composition and close to the adiabatic temperature, as would be the case if the whole core were vigorously convecting: the temperature of the reference state is determined by the adiabatic gradient for the liquid iron mixture of the core and the solidus temperature at the inner core boundary (ICB). Cooling on the adiabat leads to freezing at the ICB, as originally envisaged by Jacobs (1953); this freezing liberates latent heat due to the phase change (Verhoogen, 1961) and releases a light component of the liquid, probably oxygen (Alfè et al., 1999b), that does not form part of the solid lattice (Braginsky, 1963). This light component is assumed to be mixed throughout the outer core by the convection: none passes across the CMB into the mantle. Additionally, we allow for the possibility of heating within the core due to the presence of radiogenic elements such as potassium (e.g. Nimmo et al., 2004).

The following mathematical description of the reference state is taken from Gubbins et al. (2004), where further details may be found. Symbols are defined in Table 1. The quantity $T_\mathrm{a}^{-1}(r,t)\partial T_\mathrm{a}(r,t)/\partial t$, where $T_\mathrm{a}(r,t)$ is the adiabatic temperature, is independent of radius to a very good approximation [it neglects changes in g, γ, and ϕ in (11) caused by the cooling] and may therefore be expressed in terms of the cooling rate at the CMB:

$$\frac{\partial T_\mathrm{a}(r,t)}{\partial t} = \frac{T_\mathrm{a}\,(r,t)}{T_\mathrm{o}}\frac{dT_\mathrm{o}}{dt}. \tag{1}$$

Cooling releases heat at the rate $\bar{\rho} C_p \partial T/\partial t$; since T here is close to the adiabatic temperature we may relate it simply to the surface cooling rate

$$q_s = \bar{\rho} C_p \frac{T_\mathrm{a}(r_\mathrm{o},t)}{T_\mathrm{o}}\frac{dT_\mathrm{o}}{dt}. \tag{2}$$

The inner core radius increases at a rate

$$\frac{dr_\mathrm{i}}{dt} = \frac{1}{\tau_r}\frac{T_\mathrm{i}}{T_\mathrm{o}}\frac{dT_\mathrm{o}}{dt}, \tag{3}$$

where τ_r is the difference between the melting and adiabatic gradients at the ICB and, like the cooling rate, is negative (Table 1). Latent heat released at the ICB is therefore simply

$$q_L^{(S)} = \frac{\rho_{\rm i} L}{\tau_r} \frac{T_{\rm i}}{T_{\rm o}} \frac{dT_{\rm o}}{dt} \tag{4}$$

(note that this is a heat per unit area, not per unit volume). Light elements are released at the ICB at a rate $\rho_{\rm i} c_o dr_{\rm i}/dt$ kgm^{-2}s^{-1}. This mass is redistributed uniformly throughout the outer core, leading to a slow uniform increase of concentration given by

$$s_c = \bar{\rho}\frac{dc}{dt} = \bar{\rho}\frac{4\pi r_{\rm i}^2 \rho_{\rm i} c_0}{M_{\rm oc}}\frac{dr_{\rm i}}{dt} = \bar{\rho}\frac{4\pi r_{\rm i}^2 \rho_{\rm i} c_0}{\tau_r M_{\rm oc}}\frac{T_{\rm i}}{T_{\rm o}}\frac{dT_{\rm o}}{dt}. \tag{5}$$

Radiogenic heating, $q_{\rm r}$, is constant because the radiogenic isotopes can be assumed to be well-mixed by the convection. Other terms are neglected; these include the heat of reaction, which is equivalent to small changes in the latent heat.

Now consider typical numerical geodynamo simulations. These involve solving for departures from a well-mixed hydrostatic reference state, which is assumed to be time-independent over the timescales associated with the convection. In the Boussinesq approximation all compressibility effects are ignored except for buoyancy forces and the adiabatic temperature of the reference state*. This approximation is self-consistent provided we also omit stress heating (Spiegel & Veronis, 1960; Mihaljan, 1962; Hewitt et al., 1975); in the context of a geodynamo simulation this requires omission of the ohmic and viscous heating from the temperature equation, and neglecting in the mass transport equation the heat arising from the gravitational energy change that accompanies release and redistribution of light material as the inner core freezes (Anufriev et al., 2005). The Boussinesq equations are formed by subtracting the adiabatic temperature and hydrostatic pressure of the reference state, which creates an equivalent volumetric heat sink in the heat equation: this is the heat lost to convection by conduction down the adiabat. A similar procedure is needed for the mass diffusion equation because some light material is carried upwards by *barodiffusion*, the tendency of light material to migrate down the pressure gradient. This flux must be subtracted from the mass diffusion equation, yielding a Boussinesq equation with a volumetric mass sink. The diffused light material is lost to convection.

The equations for the temperature, T, and light element fraction, c, are

$$\bar{\rho} C_p \frac{DT}{Dt} - k\nabla^2 T \quad = \quad q, \tag{6}$$

---

* Some authors reserve the term "Boussinesq" for a more restricted approximation with no adiabat. We use the extended form. A similar approach works for the anelastic approximation, which has the advantage of including the stress heating in the solution.

$$\bar{\rho}\frac{Dc}{Dt} + \nabla \cdot \boldsymbol{i} \quad = \quad 0, \tag{7}$$

where $\boldsymbol{i}$ is the mass flux of light material and q is any heat source per unit volume that may be present. In the reference state $D/Dt = 0$ and $T = T_{\mathrm{a}}$, the adiabatic temperature. Subtracting T_{a} introduces a volumetric heat sink

$$q_{\mathrm{a}} = -k\nabla^2 T_{\mathrm{a}} \tag{8}$$

into the Boussinesq temperature equation. Fick's law for the mass flux gives

$$\boldsymbol{i} = -\bar{\rho}D\nabla c + \alpha_c \alpha_D \boldsymbol{g}, \tag{9}$$

where thermodiffusion has been neglected. The first term on the right hand side represents the usual molecular diffusion of light material, the second barodiffusion down the steep hydrostatic pressure gradient, $-\bar{\rho}\boldsymbol{g}$ (Gubbins et al., 2004). The reference state is well-mixed and therefore $\nabla c = 0$; subtracting the barodiffusive flux therefore gives rise to a volumetric mass sink of the form

$$s_{\mathrm{b}} = \alpha_c \alpha_D \nabla \cdot \boldsymbol{g}. \tag{10}$$

The buoyancy profile of the reference state is determined by the sources and sinks described above. The sources of buoyancy are the D/Dt terms in (6) and (7), which represent the secular change of the reference state with time and give rise to specific heat and mass sink contributions to the Boussinesq equations as given by (2) and (5), together with contributions from the latent heat given by (4) and any radiogenic heating. The sinks of buoyancy are due to the adiabat and the barodiffusion as defined in equations (8) and (10). The dynamo calculation solves for departures from the reference state.

The Boussinesq equations require boundary conditions as well as volumetric heat or mass sources, which are discussed in detail by Braginsky & Roberts (1995) and Anufriev et al. (2005). At the CMB we shall assume a fixed temperature gradient dT/dr, and zero mass flux, $\boldsymbol{i} = 0$. The latter condition reduces to a fixed concentration gradient dc/dr at the CMB because $dc/dr|_{r=r_{\mathrm{o}}}$ must balance the barodiffusion gradient there (as can be seen by setting $\boldsymbol{i} = 0$ in (9)); physically it corresponds to a higher concentration of light elements on the mantle side of the CMB than the core side. At the ICB the temperature and composition are linked because the compositional flux is determined by the rate of melting, which in turn depends on the convective heat-flux. There is no simple way to accommodate this boundary condition short of solving the dynamo problem with two diffusion equations, one for temperature and one for composition, as done by Glatzmaier & Roberts (1996) and Manglik et al. (2010). In this initial study we wish to avoid the complication of two diffusion equations and consider constant temperature and concentration on the lower boundary.

It is often convenient to subtract out the temperature and composition of a *basic state of rest* that satisfies the diffusion equations and boundary conditions. These conduction solutions can be chosen, if required, to remove the volumetric sources completely from the Boussinesq equations and make the boundary conditions homogeneous. Although this is not implemented in our code, we use it here to provide a convenient way to compare different heat and compositional driving sources for the convection. Plotting the various contributions to these basic conduction state temperatures and compositions as functions of radius allows quantitative comparison of each source of buoyancy.

The paper is organised as follows. In Section 2 we derive expressions for the individual contributions to the buoyancy profile described above using equations from core energetics studies (e.g. Gubbins et al., 1979; Braginsky & Roberts, 1995; Buffett et al., 1996; Labrosse et al., 1997; Gubbins et al., 2004; Nimmo, 2007). We combine the buoyancy effects of composition and temperature into a single cotemperature by converting compositional effects into equivalent heat sources/sinks, which allows us to compare the strength of the two contributions and to discuss the results of geodynamo simulations in the context of purely thermal convection. The resulting cotemperature profiles depend on parameters that are estimated from seismology and/or mineral physics with two exceptions: the rate of radiogenic heat production and the cooling rate at the CMB, both of which can be obtained from core energetics studies. Different values of these two parameters correspond to different thermochemical histories for the core, which we refer to as *core evolution scenarios*. This two-parameter formulation allows us to directly use outputs from core energetics studies to evaluate individual terms in the buoyancy profile. In Section 3 we produce buoyancy profiles for 3 end-member core evolution scenarios evaluated at the present day and make quantitative comparisons between the shapes and amplitudes of each of the sources of buoyancy. We derive the nondimensional input parameters needed by a set of purely thermally-driven convection dynamo equations that reflects all the sources of buoyancy and justify a necessary modification to bring the Rayleigh numbers into the range of numerically tractable problems. In Section 4 we conduct an initial parameter exploration for geodynamo simulations corresponding to the three core evolution scenarios, discussing the generated magnetic and velocity fields and implications for the geodynamo and core evolution. Concluding remarks are made in Section 5.

2 BUOYANCY PROFILES FOR THE EARTH'S CORE

The adiabatic gradient satisfies the equation

$$T_{\rm a}(r) = T_{\rm o} \exp\left(\int_r^{r_{\rm o}} \frac{g\gamma}{\phi} dr\right), \tag{11}$$

where γ is the Grüneissen constant, g the acceleration due to gravity, and ϕ the seismic parameter. We approximate g with $g_0 r$, where g_0 is a constant, as in many geodynamo calculations. We also take γ to be constant, as shown by first principles calculations (Alfè et al., 1999a), and ϕ to be constant, a common but weaker approximation. Doing the integral and expanding the exponential while retaining only the first two terms gives a quadratic expression for the adiabatic gradient [see also Labrosse et al. (1997)]: $T_{\rm a}(r) = A - Br^2$. The constants are most conveniently expressed in terms of the temperatures at the ICB and CMB to give a good approximation to the full expression for the adiabat:

$$T_{\rm a}(r) = T_{\rm i} - \frac{(T_{\rm i} - T_{\rm o})}{(r_{\rm o}^2 - r_{\rm i}^2)}\left(r^2 - r_{\rm i}^2\right) = \frac{1}{(r_{\rm o}^2 - r_{\rm i}^2)}[(T_{\rm i} r_{\rm o}^2 - T_{\rm o} r_{\rm i}^2) - (T_{\rm i} - T_{\rm o})r^2]. \tag{12}$$

This quadratic approximation differs by less than 8 K from the full calculation using PREM parameters. It has the advantage of producing a uniform equivalent heat sink because $\nabla^2(A - Br^2) = -6B$. Physically, q_a may be regarded as the heat conducted away from the fluid at a particular location; it does not need to be transported by the convection. Geometrically, this term causes the amount of heat conducted down the adiabat to increase with radial distance from the geocentre; less of the input heating is available to drive convection in the upper layers. This adiabatic effective heat sink, called the *heat-flux deficit* by Anufriev et al. (2005), is significant, comparable with other heat source terms.

The barodiffusive flux varies as $g \approx g_0 r$ and therefore increases with radius if α_c and α_D can be taken as constants; the gradient steepens towards the CMB like the adiabat. The equivalent mass sink is uniform: $s_{\rm b} = 3\alpha_c \alpha_D g_0$.

Temperature and concentration are combined into a *cotemperature*

$$T_{\rm co} = T + \frac{\alpha_c}{\alpha_T} c \tag{13}$$

so that the buoyancy force becomes $\bar{\rho}\alpha_T T_{\rm co}$, the same form as for thermal convection. Cotemperature is very similar to the codensity (Braginsky & Roberts, 1995) that has been widely used in geodynamo models (e.g. Aubert et al., 2009; Olson et al., 2010), but converts compositional effects into equivalent thermal effects; this allows us to compare quantitatively the separate contributions of temperature and compositional sources of buoyancy by multiplying c by the ratio of expansion coefficients. To complete the cotemperature transformation we need to combine the two diffusion equations (6) and (7) into one. Multiplying (7) by $C_p(\alpha_c/\alpha_T)$ and using Fick's law (9) for the mass flux gives

$$\bar{\rho} C_p \frac{D}{Dt}\left(\frac{\alpha_c}{\alpha_T} c\right) - \bar{\rho} C_p D \nabla^2 \left(\frac{\alpha_c}{\alpha_T} c\right) - C_p \frac{\alpha_c}{\alpha_T} s_{\rm b} = 0. \tag{14}$$

Adding this to the thermal diffusion equation (6) gives a diffusion equation for the cotemperature provided the diffusivities are the same, i.e. $D = k/\bar{\rho} C_p = \kappa$

$$\frac{DT_{\rm co}}{Dt} - \kappa \nabla^2 T_{\rm co} = \frac{q}{\bar{\rho} C_p} + \frac{s_{\rm b}}{\rho}\frac{\alpha_c}{\alpha_T}. \tag{15}$$

This equation allows us to perform geodynamo simulations in exactly the same way as we would for pure thermal convection. It also shows us how to compare the buoyancy effects of volumetric sources of composition (s) and heat (q)—multiply the former by $C_p\alpha_c/\alpha_T$. Boundary conditions on T and c must also be the same, which we have arranged, so (15) is subject to fixed cotemperature on the bottom and fixed gradient (flux) at the top. The molecular diffusivities κ and D are not the same; they differ by 2 orders of magnitude. Equalising them removes doubly-diffusive effects, which we regard as an unnecessary complication at this stage. Furthermore, numerical calculations invariably replace molecular diffusivities with much larger, closely similar, turbulent values: our equalisation of diffusivities is not therefore too severe an additional restriction. Of course, molecular diffusivities are relevant when calculating heat-flux down the adiabat and barodiffusive mass flux; turbulent diffusivities only apply to the departures from the reference and basic states. Molecular diffusivities are also necessary if any part of the core is stably stratified (Manglik et al., 2010), but we do not consider this situation.

We remove a basic state of rest from (15) and transfer the D/Dt terms associated with the slow evolution of the reference state to the right-hand side (Kono & Roberts, 2001). Equation (15) can then be written in the form

$$-\kappa \nabla^2 T_{\rm co} = q = q_{\rm s} + q_c + q_{\rm r} + q_{\rm a} + q_{\rm b}, \tag{16}$$

where the volumetric heat sources and sinks are:

$$q_{\rm a} = -k\nabla^2 T_{\rm a} = -6k\frac{(T_{\rm i} - T_{\rm o})}{(r_{\rm o}^2 - r_{\rm i}^2)}, \tag{17}$$

$$q_{\rm r} = \text{constant}, \tag{18}$$

$$q_c = -\bar{\rho} C_p \frac{\alpha_c}{\alpha_T}\frac{4\pi r_{\rm i}^2 \rho_{\rm i} c_0}{\tau_r M_{\rm oc}}\frac{T_{\rm i}}{T_{\rm o}}\frac{dT_{\rm o}}{dt}, \tag{19}$$

$$q_{\rm s} = -\frac{\bar{\rho} C_p}{(r_{\rm o}^2 - r_{\rm i}^2)}[(T_{\rm i} r_{\rm o}^2 - T_{\rm o} r_{\rm i}^2) - (T_{\rm i} - T_{\rm o}) r^2]\frac{1}{T_{\rm o}}\frac{dT_{\rm o}}{dt}, \tag{20}$$

$$q_{\rm L} = 0, \tag{21}$$

$$q_{\rm b} = -3\frac{\alpha_c^2}{\alpha_T} C_p \alpha_D g_0. \tag{22}$$

The total heat flows are

$$
\begin{aligned}
Q_{\mathrm{a}} &= -8\pi r_{\mathrm{o}}^3 k \frac{(T_{\mathrm{i}} - T_{\mathrm{o}})}{(r_{\mathrm{o}}^2 - r_{\mathrm{i}}^2)}, && (23)\\
Q_{\mathrm{r}} &= q_{\mathrm{r}} V_{\mathrm{oc}}, && (24)\\
Q_c &= -\bar{\rho} C_p \frac{\alpha_c}{\alpha_T} \frac{4\pi r_{\mathrm{i}}^2 \rho_{\mathrm{i}} c_0}{\tau_r M_{\mathrm{oc}}} \frac{T_{\mathrm{i}}}{T_{\mathrm{o}}} \frac{dT_{\mathrm{o}}}{dt} V_{\mathrm{oc}}, && (25)\\
Q_s &= -\bar{\rho} C_p \frac{4\pi r_{\mathrm{o}}^2}{(r_{\mathrm{o}}^2 - r_{\mathrm{i}}^2)} \left[\frac{1}{3}(T_{\mathrm{i}} r_{\mathrm{o}}^2 - T_{\mathrm{o}} r_{\mathrm{i}}^2) r_{\mathrm{o}} - \frac{1}{5}(T_{\mathrm{i}} - T_{\mathrm{o}}) r_{\mathrm{o}}^3 \right] \frac{1}{T_{\mathrm{o}}} \frac{dT_{\mathrm{o}}}{dt}, && (26)\\
Q_{\mathrm{L}} &= \frac{4\pi r_{\mathrm{i}}^2}{\tau_r} \rho_{\mathrm{i}} L \frac{T_{\mathrm{i}}}{T_{\mathrm{o}}} \frac{dT_{\mathrm{o}}}{dt}, && (27)\\
Q_{\mathrm{b}} &= -3 \frac{\alpha_c^2}{\alpha_T} C_p \alpha_D g_0 V_{\mathrm{oc}}. && (28)
\end{aligned}
$$

Local heat per unit volume is denoted q (measured in Wm^{-3}), compositional sources by s (measured in m^{-3}) and total heat by Q. Subscripts are s,L,c,a,r for specific heat, latent heat, composition, adiabat and radioactivity. Superscript S denotes flux per unit area.

Radioactivity gives a simple uniform heat source q_{r} provided by the specific core evolution scenario. The adiabatic heat sink, q_{a} in (8), is also uniform thanks to our linear approximation to the adiabatic gradient; it depends only on core properties. The equivalent heat source for the compositional sink, q_{c}, is obtained by comparing terms on the right hand side of (13) and substituting the mass sink from (5) to give (19). It depends on the cooling rate at the CMB, dT_{o}/dt. Specific heat is not uniform because it is proportional to the adiabatic temperature T_{a}, which varies quadratically (equation (12)): q_{s} decreases with radius. It is therefore more efficient at driving convection than uniform heating because more heat is released at depth where the temperature is higher, thus contributing more to the entropy balance. The quadratic part in (20) is only a small fraction of the constant part (4%) at the ICB but rises to 40% at the CMB. The latent heat has no volumetric heating; it is determined by the boundary conditions. It is the most efficient form of heating in that all of the heat is released at the hottest temperature in the system and removed at the coldest temperature, thus contributing more entropy than any other form of heating. Specific and latent heats depend also on the core evolution scenario through the CMB cooling rate. The barodiffusive equivalent heat-flux, q_{b}, is obtained from s_{b} by multiplying by $C_p \alpha_c/\alpha_T$, as required to bring (7) into line with (6).

Comparing q's tells us where the heat sources and sinks are but not how strongly the convection is driven at a particular radius because this also depends on the boundary conditions. The superadiabatic temperature gradient of the basic state is a better measure of the relative convective driving at different depths. It is readily calculated by solving the conduction equation with the appropriate boundary conditions. Each basic state temperature profile must satisfy the upper fixed gradient condition on the CMB. The lower temperature boundary condition is redundant: it only serves to determine the temperature. The upper boundary condition is

$$-\oint \kappa \nabla T_{\mathrm{co}} \cdot d\mathbf{S} = Q_s + Q_{\mathrm{r}} + Q_{\mathrm{L}} + Q_{\mathrm{a}} + Q_{\mathrm{b}}. \tag{29}$$

For each Q the corresponding temperature gradient is $T'(r_{\mathrm{o}}) = Q/4\pi r_{\mathrm{o}}^2 k$, where prime denotes d/dr. When the heat source is distributed throughout the inner core as well as the outer core, as is the case with specific and radiogenic heat, the constant of integration is determined by regularity at the origin and the upper boundary condition is satisfied automatically.

The uniform heat sources, q_{r}, q_c and q_{b}, have linear temperature gradients. The adiabatic gradient is obtained simply by differentiating (12). Specific heat is a little more complicated because the source is quadratic and the temperature gradient involves an r^3 term in addition to the usual r from the uniform part of the heating; it rises from 2% of the linear term at the ICB to 17% at the CMB. Latent heat gives a temperature gradient proportional to r^{-2}. All these quantities provide input to the Boussinesq equations, which uses turbulent thermal rather than molecular diffusivity; they must therefore be expressed in terms of the turbulent diffusivity or thermal conductivity $k_{\mathrm{T}} = \bar{\rho} C_P \kappa_{\mathrm{T}}$. The resulting temperature gradients are:

$$T'_{\mathrm{a}} = -2\frac{k}{k_{\mathrm{T}}}\frac{(T_{\mathrm{i}} - T_{\mathrm{o}})}{(r_{\mathrm{o}}^2 - r_{\mathrm{i}}^2)} r, \tag{30}$$

$$T'_{\mathrm{r}} = \frac{q_{\mathrm{r}}}{3k_{\mathrm{T}}} r, \tag{31}$$

$$T'_{\mathrm{c}} = -\frac{1}{3\kappa_{\mathrm{T}}}\frac{\alpha_c}{\alpha_T}\frac{4\pi r_{\mathrm{i}}^2 \rho_{\mathrm{i}} c_0}{\tau_r M_{\mathrm{oc}}}\frac{T_{\mathrm{i}}}{T_{\mathrm{o}}}\frac{dT_{\mathrm{o}}}{dt}\left(r - \frac{r_{\mathrm{o}}^3}{r^2}\right), \tag{32}$$

$$T'_{\mathrm{s}} = -\frac{1}{\kappa_{\mathrm{T}}(r_{\mathrm{o}}^2 - r_{\mathrm{i}}^2)}\left[\frac{1}{3}(T_{\mathrm{i}} r_{\mathrm{o}}^2 - T_{\mathrm{o}} r_{\mathrm{i}}^2) r - \frac{1}{5}(T_{\mathrm{i}} - T_{\mathrm{o}}) r^3\right]\frac{1}{T_{\mathrm{o}}}\frac{dT_{\mathrm{o}}}{dt}, \tag{33}$$

$$T'_{\mathrm{L}} = \frac{\rho_{\mathrm{i}} L}{\tau_r k_{\mathrm{T}}}\frac{T_{\mathrm{i}}}{T_{\mathrm{o}}}\frac{dT_{\mathrm{o}}}{dt}\frac{r_{\mathrm{i}}^2}{r^2}, \tag{34}$$

$$T'_{\mathrm{b}} = -\frac{\alpha_c^2 \alpha_D g_0}{\alpha_T \bar{\rho} \kappa_{\mathrm{T}}} r. \tag{35}$$

3 INPUT PARAMETERS FOR THE GEODYNAMO CALCULATIONS: NUMERICAL VALUES

We use three scenarios for core evolution taken from Gubbins et al. (2004) and summarised in Table 2. All have ICB density jump 0.59 Mgm^{-3} and Cases 1, 2 and 3 in this paper correspond to Models (i), (ii), and (v) in Table 5 of Gubbins et al. (2004). Case 1 has a rapid cooling rate, high CMB heat flow and a young inner core. Case 2 has a lower cooling rate and a total CMB heat flow equal to the adiabatic heat-flux: the top of the core is thermally neutrally buoyant.

dT_{o}/dt	CMB cooling rate	KGyr^{-1}
h	radiogenic heating by mass	Wkg^{-1}
Q	total heat-flux	W
q	volumetric heat source	Wm^{-3}
T	temperature	K
s	volumetric mass source	$\mathrm{kgm}^{-3}\mathrm{s}^{-1}$
β	coefficient of conduction temperature profile	
c	concentration of light material	
$\boldsymbol{i}$	mass flux	$\mathrm{kgm}^{-2}\mathrm{s}^{-1}$
r_{i}	inner core radius	1.221×10^{6} m
r_{o}	outer core radius	3.485×10^{6} m
V_{oc}	volume of outer core	$1.70 \times 10^{20}\ \mathrm{m}^{3}$
M_{oc}	mass of outer core	1.85×10^{24} kg
$\bar{\rho}$	mean outer core density	$10.9\ \mathrm{Mgm}^{-3}$
ρ_{i}	ICB density	$12.2\ \mathrm{Mgm}^{-3}$
g	acceleration due to gravity	$10\ \mathrm{ms}^{-2}$
g_0	$\approx g(r)/r$	$3.25\times10^{-6}\ \mathrm{s}^{-2}$
T_{o}	outer core temperature	4040 K
T_{i}	inner core temperature	5500 K
k	thermal conductivity	$50\ \mathrm{Wm}^{-1}\mathrm{K}^{-1}$
C_P	specific heat at constant pressure	$840\ \mathrm{Jkg}^{-1}\mathrm{K}^{-1}$
L	latent heat of outer core liquid	$0.75 \times 10^{6}\ \mathrm{Jkg}^{-1}$
α_T	coefficient of thermal expansion	$1.35 \times 10^{-5}\ \mathrm{K}^{-1}$
α_c	compositional expansion coefficient	1.10
α_D	coefficient	$0.70 \times 10^{-12}\ \mathrm{kgm}^{-3}\mathrm{s}$
τ_r	difference between melting and adiabatic gradients	$-1.66 \times 10^{-4}\ \mathrm{Km}^{-1}$
c_0	mean outer core concentration	0.0252
κ	thermal diffusivity	$5.46 \times 10^{-6}\ \mathrm{m}^{2}\ \mathrm{s}^{-1}$
D	mass diffusivity	$10^{-8}\ \mathrm{m}^{2}\ \mathrm{s}^{-1}$
η	magnetic diffusivity	$1.6\ \mathrm{m}^{2}\ \mathrm{s}^{-1}$
ν	outer core viscosity	$10^{-6}\ \mathrm{m}^{2}\ \mathrm{s}^{-1}$
d	shell thickness $r_{\mathrm{o}} - r_{\mathrm{i}}$	2260 km
Ω	rotation rate	$7.272 \times 10^{-5}\ \mathrm{s}^{-1}$
μ_0	permeability of free space	$4\pi \times 10^{-7}\ \mathrm{Hm}^{-1}$
$\mathbf{u}$	fluid velocity	$\mathrm{m\ s}^{-1}$
$\mathbf{B}$	magnetic field	T

Table 1. Mathematical quantities and, where relevant, their numerical values used in the calculations. Generic sub- and superscripts used in the text are also listed below.

Subscripts		Superscripts	
s	secular cooling	b	bottom heating
L	latent heat	i	internal heating
a	adiabat	s	non-uniform part of secular cooling
b	barodiffusion	S	source per unit area
r	radiogenic heating	$'$	d/dr
c	composition		
co	cotemperature		
T	turbulent quantity		

Table 1. continued.

Case 3 has the same total heat-flux as Case 2 but with enough additional radiogenic heating to make the age of the inner core close to that of the Earth, 3.5 Ga. The cooling rate is much reduced over that of Case 2. These choices represent a broad spread of scenarios discussed in the literature, ranging from high to low total heat flow, inner core ages, and radiogenic heating.

The resulting volumetric equivalent and total heat-fluxes are given in Table 2; they depend on the core evolution scenario through $dT_{\rm o}/dt$ and h. All heat sources and sinks are uniform except for $q_{\rm s}$, which has been averaged over the core to give a single value for comparison with the other values. Cases 1 and 2 have net heat sinks while Case 3 has only bottom heating—the radiogenic heat almost exactly cancels the adiabatic, convective, and other heat sinks. The Q's are shown for comparison with the latent heat $Q_{\rm L}$, which has zero volumetric heat source. The compositional terms dominate in the rapidly cooling evolutions and the barodiffusive contribution is negligible.

These equivalent heat sources should not be confused with the power estimates normally made for core energetics calculations. While the radiogenic, specific, and latent heats are the same the adiabatic heat has the opposite sign because it is subtracted from the heat sources entering the Boussinesq equations. Furthermore the compositional and barodiffusive terms are the result of transforming compositional into thermal buoyancy and have nothing to do with the gravitational energy released.

Figure 1 shows the contributions to the radial variation of $T'_{\rm co}$ for Cases 1, 2 and 3. Specific and radiogenic heating increase linearly with radius while the composition and latent heat terms decrease as r^{-2} because light elements and latent heat are released at the ICB. Temperature effects are weaker than compositional effects, in agreement with core energetics calculations. The adiabatic gradient also increases linearly with radius and so the superadi-

	Case 1	Case 2	Case 3
h pWkg^{-1}	0	0	4
$dT_{\rm o}/dt$ KGyr^{-1}	123	69	12
$q_{\rm r}$ nWm^{-3}	0	0	44
$q_{\rm a}$ nWm^{-3}	-41.1	-41.1	-41.1
q_c nWm^{-3}	-74.2	-41.6	-7.2
$\bar{q}_{\rm s}$ nWm^{-3}	36.1	20.3	3.5
$q_{\rm b}$ nWm^{-3}	-0.5	-0.5	-0.5
$q_{\rm total}$ nWm^{-3}	-65.5	-54.9	0.1
$Q_{\rm L}$ TW	5.5	3.1	0.5
$Q_{\rm r}$ TW	0	0	7.4
$Q_{\rm a}$ TW	-6.9	-6.9	-6.9
Q_c TW	-12.6	-7.1	-1.2
$Q_{\rm s}$ TW	5.0	2.8	0.4
$Q_{\rm b}$ TW	0.1	0.1	0.1

Table 2. Numerical values for volumetric and total heat sources for the 3 scenarios of core evolution considered here. The radiogenic heating, h, and rate of drop of temperature at the CMB, $dT_{\rm o}/dt$, define the evolution. Other parameters are given in Table 1. Adiabatic and barodiffusive heating do not depend on core evolution and are the same in each Case. All q's are independent of r except $q_{\rm s}$, which has been averaged over the core to give a single number.

abatic gradient reduces near the CMB for all Cases. The small barodiffusive term is similar but too small to be plotted. In all Cases the gradients are much larger at depth in the core than near the CMB.

Composition clearly dominates in all Cases, even when substantial radiogenic heating is incorporated. For Case 1 the buoyancy profile is dominated by sources near the ICB with the cotemperature gradient decreasing by a factor of 50 between the ICB and CMB. For Case 2 composition and heat terms contribute in roughly equal amounts. The buoyancy profile is again dominated by sources near the ICB with the cotemperature gradient decreasing by a factor of 20 between the ICB and CMB. In Case 3 the radiogenic heat is greater than any other heat source and the buoyancy profile is much flatter. The cotemperature gradient still decreases by a factor of 5 between the ICB and CMB but starts to flatten out near the middle of the core due to the radiogenic contribution. In all Cases convection is driven most vigorously at the bottom of the core and is barely superadiabatic at the top.

To compare the relative amplitudes of bottom and internal buoyancy sources we write the basic state temperature gradients [(30)–(34)] in the general form

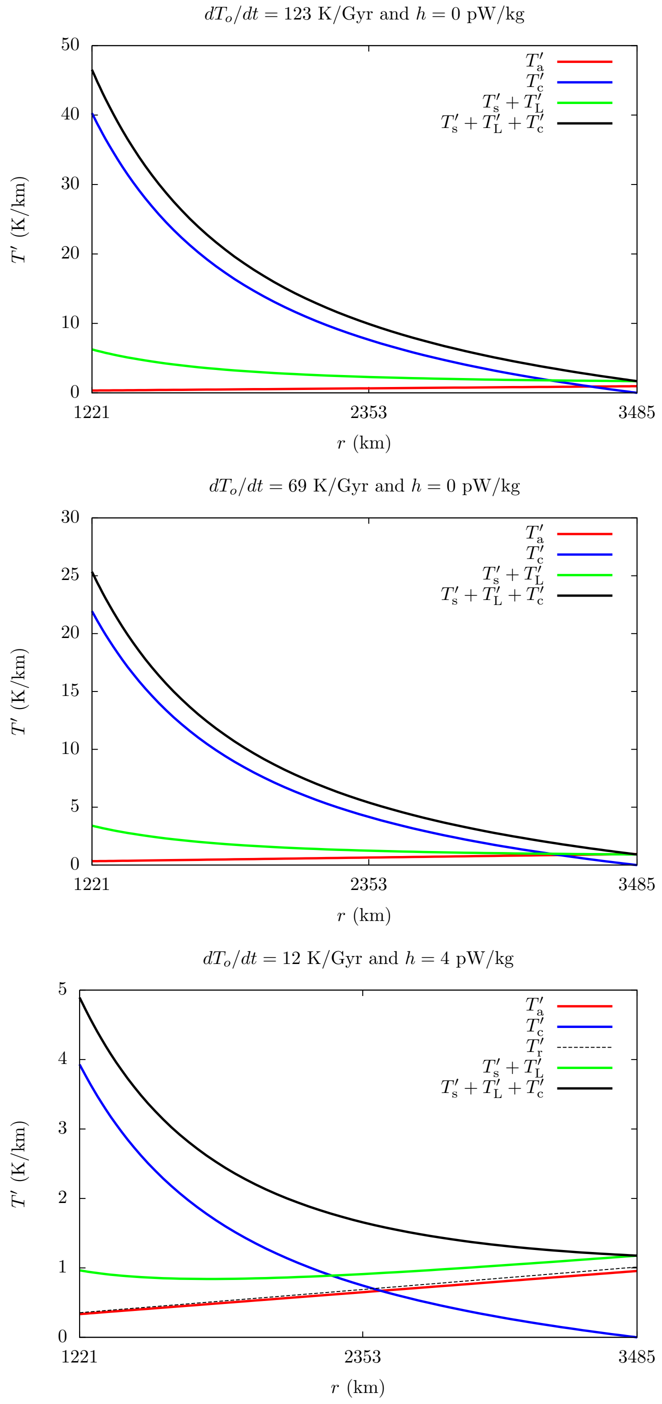

Figure 1. Variation of the applied conduction cotemperature radial gradient for the various sources and sinks of cotemperature: $T'_{\rm a}$ (red), $T'_{\rm c}$ (blue), $T'_{\rm s} + T'_{\rm L}$ (green), $T'_{\rm s} + T'_{\rm L} + T'_{\rm c}$ (thick black) and $T'_{\rm r}$ (thin black). Top: Case 1; middle: Case 2; bottom: Case 3. $T'_{\rm a}$ has been plotted positive for clarity, but it should be remembered that it is a sink while all other plotted terms are sources.

$$T'(r) = \frac{\beta^{(b)}}{r^2} + \beta^{(i)}r + \beta^{(s)}r^3, \tag{36}$$

(e.g. Kono & Roberts, 2001) where the constants β determine the amount of bottom heating, internal heating, and non-uniform part of the specific heating. These are simply derived from the corresponding temperature gradients in equations (30)–(34), replacing r with the length scale d. The results are given in Table 3. Compositional buoyancy dominates thermal buoyancy in each Case and bottom heating is greater than internal heating. Case 3 happens to have no net internal heating, which is presumably a coincidence because the core evolution scenario was not constructed with this in mind.

From now on we neglect barodiffusion; it is too small to have any effect away from boundaries. We nondimensionalise the dynamo equations with $\tau = d^2/\kappa$ for time and $\mathcal{B} = \sqrt{\mu_0 \rho \kappa \Omega}$ for magnetic field. We normalise the reference state profiles (31)–(34) by the adiabat gradient, $2d\kappa(T_\mathrm{i} - T_\mathrm{o})/\kappa_\mathrm{T}(r_\mathrm{o} + r_\mathrm{i})$ from (30) (as in (36)) and scale the total temperature by $T = \Omega\kappa/\alpha_T g_0 d^2$. In this way we can define one Rayleigh number in terms of the adiabat and relate other forms of buoyancy to it.

The resulting nondimensional equations of momentum, induction, and heat are

$$\begin{aligned} Pr^{-1}E\left[\frac{\partial \mathbf{u}}{\partial t} + (\mathbf{u}\cdot\nabla)\mathbf{u}\right] + 2\hat{\mathbf{\Omega}} \times \mathbf{u} &= -\nabla P + T\boldsymbol{r} + (\nabla \times \mathbf{B}) \times \mathbf{B} + E\nabla^2\mathbf{u}, && (37)\\ \frac{\partial \mathbf{B}}{\partial t} &= \nabla \times (\mathbf{u} \times \mathbf{B}) + \frac{Pr}{Pm}\nabla^2\mathbf{B}, && (38)\\ \frac{\partial T}{\partial t} + (\mathbf{u}\cdot\nabla)T &= \nabla^2 T - ERa\frac{q}{q_\mathrm{a}}, && (39) \end{aligned}$$

to be solved with the usual solenoidal conditions $\nabla\cdot\mathbf{u} = \nabla\cdot\mathbf{B} = 0$. The dimensionless groups are

$$Pr = \frac{\nu_\mathrm{T}}{\kappa_\mathrm{T}}; \quad Pm = \frac{\nu_\mathrm{T}}{\eta}; \quad E = \frac{\nu_\mathrm{T}}{\Omega d^2}; \quad ERa = \frac{2\alpha_T \kappa g_0 d^3\,(T_\mathrm{i} - T_\mathrm{o})}{\Omega \kappa_\mathrm{T}^2\,(r_\mathrm{o} + r_\mathrm{i})}.$$

Ra has the form of a conventional Rayleigh number:

$$Ra = 2\frac{\alpha_T \kappa g_0 d^5\,(T_\mathrm{i} - T_\mathrm{o})}{\kappa_\mathrm{T}^2 \nu_\mathrm{T}\,(r_\mathrm{o} + r_\mathrm{i})}. \tag{40}$$

At first sight this choice of Ra seems strange because it is based on the temperature scale $(T_\mathrm{i} - T_\mathrm{o})$, which has nothing to do with the Boussinesq equations: it actually measures the extent to which the adiabat reduces convection by the heat deficit. However, unlike q/q_a, it depends only on core properties and not on the model parameters dT_o/dt and h and so does not vary between core evolution scenarios. Furthermore, realistic values of Ra are not achievable in numerical geodynamo simulations whereas realistic ratios of q/q_a are.

Putting in numerical values from Table 1 gives $Ra = 2.16 \times 10^{12}$. This may seem high but it is not for rotation as rapid as the Earth's. The critical Rayleigh number for rapidly rotating

	Case 1			Case 2			Case 3		
	$dT_\mathrm{o}/dt = 123$ K/Gyr $h = 0$			$dT_\mathrm{o}/dt = 69$ K/Gyr $h = 0$			$dT_\mathrm{o}/dt = 12$ K/Gyr $h = 4$ pW/kg		
	$\beta^{(b)}$	$\beta^{(i)}$	$\beta^{(s)}$	$\beta^{(b)}$	$\beta^{(i)}$	$\beta^{(s)}$	$\beta^{(b)}$	$\beta^{(i)}$	$\beta^{(s)}$
a	0	-1	0	0	-1	0	0	-1	0
r	0	0	0	0	0	0	0	1.06	0
c	6.59	-1.90	0	3.70	-1.10	0	0.64	-0.18	0
s	0	1.23	-0.09	0	0.69	-0.05	0	0.12	-0.01
L	2.74	0	0	1.54	0	0	0.27	0	0
Total	9.33	-1.67	-0.09	5.24	-1.4	-0.05	0.91	0.00	-0.01

Table 3. Numerical values for the dimensionless constants appearing in the equation for the conduction temperature (36), $\beta_a^{(i)}$ etc, normalised by the adiabatic value. Note that the r^3 term in the specific heat, $\beta_s^{(s)}$, is small enough to be neglected, leaving a combination of bottom and uniform internal heating. Case 3, which has a large amount of radiogenic heating, happens to have virtually no net internal heating. Compositional contributions (subscript c) dominate thermal contributions.

convection scales as $Ra^c = O(E^{-4/3})$ and for magnetoconvection as $O(E^{-1})$ (Chandrasekhar, 1961). For nonmagnetic convection the constant depends on the Prandtl number but is of order unity for moderate Pr (Zhang, 1992); for magnetoconvection Ra^c depends critically on the applied magnetic field and the results are harder to apply to a dynamo where the field is self-generated. For turbulent diffusivities $E = 10^{-9}$ giving $Ra^c = O(10^{12})$ for nonmagnetic convection and $O(10^9)$ for magnetoconvection. Therefore, if turbulent diffusivities are relevant to the Earth, then the geodynamo is operating at a Rayleigh number that is near to critical for nonmagnetic convection or a thousand times critical for magnetoconvection, as found by Gubbins (2001) using a similar argument and, independently, by Jones (2000), whose estimate is based on the speed of fluid motions inferred at the top of the core. It would be wrong to use the Earth's value for Ra (2.16×10^{12}) in a geodynamo simulation with radically different Ekman number ($E = 10^{-4}$ rather than $E = 10^{-9}$). The best option is to keep the Rayleigh number about the same in relation to the critical Rayleigh number for the value of E used. In this study we have kept Ra rather low but above critical and use ERa, sometimes called the modified Rayleigh number, as a convenient measure. We draw no conclusions from the absolute values used for Ra, only for the relative mix of bottom and internal heating.

4 GEODYNAMO MODELS

We have conducted a preliminary study to demonstrate the effects of different buoyancy profiles by varying ERa and fixing the nondimensional numbers $E = 10^{-4}$ and $Pr = Pm = 1$, which allowed many runs to be performed for each Case. For all models no-slip velocity boundary conditions are applied at both boundaries. The inner boundary is held at a fixed temperature and concentration and is electrically conducting, while at the outer boundary the heat-flux is fixed, the mass flux is zero and the magnetic field is matched to an external potential field. Models at lower values of ERa were run with 60 radial points and spherical harmonic coefficients up to degree and order 48; runs at the higher ERa were run with 150 radial points and spherical harmonic coefficients up to degree and order 128. No azimuthal symmetry was assumed and all runs exhibited a decay in the magnetic l-spectrum of at least two orders of magnitude between wavenumbers with highest and lowest energy.

A detailed description of the code implementation is given in Willis et al. (2007); it reproduces the dynamo benchmark (Christensen et al., 2001). The buoyancy profile is implemented by specifying the total outer boundary heat-flux using equations (23)–(28) in equation (29) and the total internal source/sink using equations (17)–(22) in equation (16). The Cases differ by the values of the total internal source/sink and also the outer boundary condition, which depends on the total heat source. It is important to note that it is not possible to transform a buoyancy profile obtained from one core evolution scenario into an equivalent profile obtained from a different evolution scenario simply by changing the value of ERa; models from different Cases can be scaled to make the internal sources/sinks of equal magnitude, but the the outer boundary heat-flux will not be the same (the converse is also true).

Global time-averaged properties of the solutions are given in Table 4. In Cases 1 and 3 the models exhibit the familiar transitions as a function of ERa, from stable dipolar dynamos at low ERa, through reversing dipolar dynamos to reversing multipolar dynamos at high ERa (Christensen & Aubert, 2006; Olson & Christensen, 2006). Conversely, models for Case 2 are always non-reversing and dipolar, which is probably because the transition between reversing and non-reversing dynamos for this heating mode occurs at higher Rayleigh numbers than we have considered. As ERa increases there is a general decrease in the toroidal and symmetric components of the kinetic energy, a decrease in toroidal magnetic energy and an increase in the symmetric component of the magnetic energy. For all dynamos the Elsasser number Λ, the ratio of Lorentz and Coriolis forces, is $O(1)$ as it is thought to be in the Earth (e.g. Zhang & Schubert, 2000). For detailed analysis we choose three models from each Case corresponding to low $ERa(= 10)$, intermediate $ERa(= 50)$ and high $ERa(= 200)$; time-averaged energy

Case	ERa	T	$KE_{\mathcal{T}}/KE$	$KE_{\mathcal{S}}/KE$	$ME_{\mathcal{T}}/ME$	$ME_{\mathcal{S}}/ME$	Λ	Field
1-1	10	10	72.3	79.4	58.6	31.9	2.6	N D
1-2	20	5	68.3	77.3	55.9	37.0	2.7	N D
1-3	50	2	66.4	79.5	54.7	42.4	3.7	N D
1-4	100	1	65.3	77.0	54.1	44.6	3.7	Y D
1-5	200	1	65.1	76.2	58.1	45.4	4.2	Y M
2-1	10			No dynamo				
2-2	20	5	81.1	93.9	64.9	20.7	0.79	N D
2-3	50	2	75.9	84.3	60.2	28.4	1.5	N D
2-4	100	1	69.9	81.3	58.6	34.4	1.6	N D
2-5	200	1	67.4	80.3	57.9	42.4	1.4	N D
3-1	10	10	78.7	92.6	61.8	18.4	1.3	N D
3-2	20	5	73.1	81.9	57.0	30.2	2.8	N D
3-3	50	2	70.2	78.4	56.9	33.1	3.0	N D
3-4	100	1	68.9	77.9	54.6	35.7	3.0	Y D
3-5	200	1	65.4	70.1	57.9	50.6	1.2	Y M

Table 4. Geodynamo models described in the text. The second column gives the time T in units of the magnetic diffusion time $d^2/\eta \approx 100,000$yrs over which the results have been averaged; it excludes a short transient period at the start of each model. The dimensionless kinetic (KE) and magnetic (ME) energies are given by $KE = 1/2 \int \mathbf{u}^2 dV$ and $ME = Pr/(2E) \int \mathbf{B}^2 dV$ respectively. Subscripts $\mathcal{T}$ and $\mathcal{S}$ denote respectively the energy in the toroidal and equatorially symmetric parts of the fields. The Elsasser number, $\Lambda = [2E(ME)]/Pr$. In the final column, reversing dynamos are denoted by 'Y' and non-reversing dynamos by 'N'; dipolar dynamos are denoted by 'D' and multipolar dynamos are denoted by 'M'. Numbers in columns 4–7 are percentages.

spectra for these 8 models are shown in Figure 2. In the rest of this section we refer only to thermal convection with the understanding that compositional effects are included through our use of a cotemperature.

Projections of the solutions for $ERa = 10$ are shown in Figure 3 averaged over 10 magnetic diffusion times, or approximately 1 Myr in our scaling. The minima of u_r in the equatorial plane are similar for both Cases (~ -2), but the maxima are much greater in Case 1 due to the much larger radial cotemperature gradient near the inner boundary (IB) for this Case. In both Cases there are high amplitude regions of u_r adjacent to the IB; away from the IB Case 1 exhibits localised 'patches' of high amplitude u_r, while in Case 3 there is a layer of cells near the mid-radius of the shell comprising positive and negative u_r is roughly equal proportions. This layer in Case 3 resembles the periodic array of convection cells that are

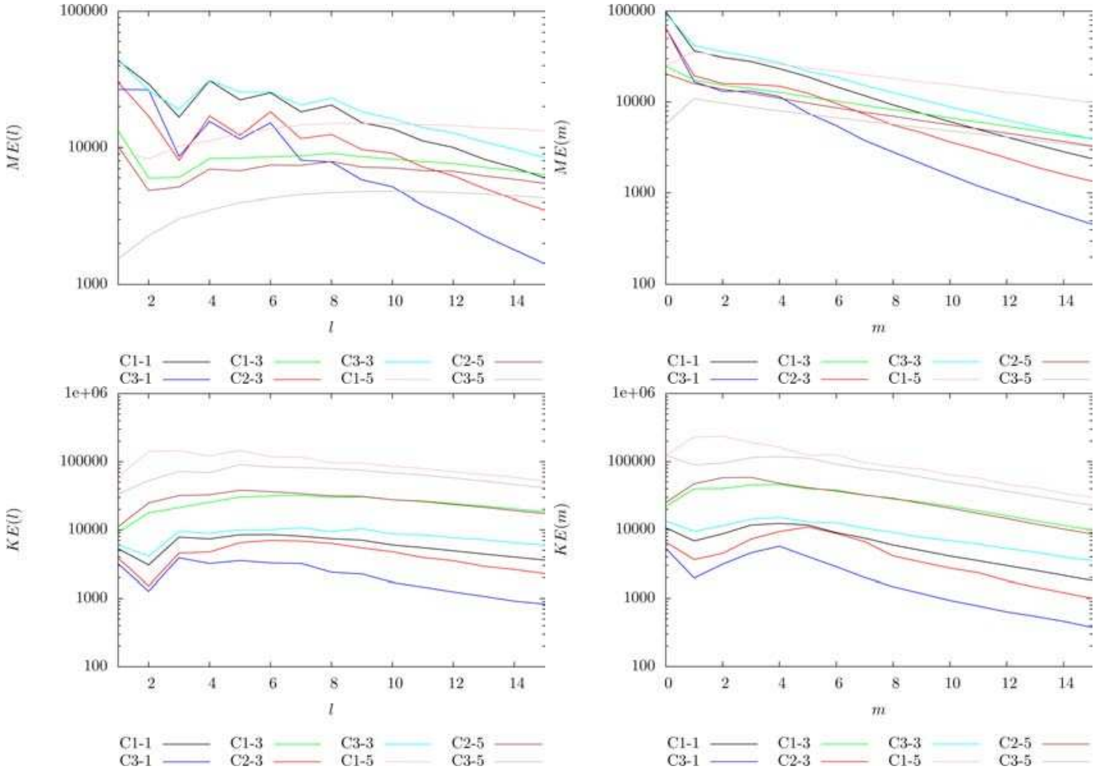

Figure 2. Time-averaged magnetic energy (top) and kinetic energy (bottom) spectra as a function of spherical harmonic degree l (left) and order m (right) up to degree and order 15.

established at the onset of instability in spherical rotating convection with purely internal heating (e.g. Busse, 1970). With purely bottom heating a periodic array of cells is established adjacent to the IB (e.g. Dormy et al., 2004) at the onset of convective instability, but it is not present in model C1-1 although this model is driven predominantly from below. The kinetic m-spectra in Figure 2 reflect these differences: for C3-1 there is a peak at $m = 4$, which is a resonance of the most unstable wavenumber ($m = 8$) for purely internal heating at $E = 10^{-4}$, while for C1-1 the spectrum is relatively flat at low wavenumbers. Equatorial sections of u_ϕ display smaller-scale structures and higher peak amplitudes for Case 1 than Case 3, which may reflect the higher ratio of $KE_{\mathcal{T}}/KE$ for model C1-1 than C3-1 in Table 4.

Meridional projections in Figure 3 show that the flow patterns are strongly columnar and equatorially symmetric as suggested by the ratio $KE_{\mathcal{S}}/KE$ in Table 4. In Case 1 there is vigorous convection inside the tangent cylinder with a strong upwelling plume near the polar axis as seen in previous models (e.g. Olson et al., 1999; Sreenivasan & Jones, 2006); this is not seen in Case 3, which may reflect the weaker buoyancy force at the IB. Meridional sections of the magnetic field show that B_r aligns with fluid downwellings in equatorial regions and fluid upwellings in polar regions (Olson et al., 1999); interestingly, the stronger columnar flows in

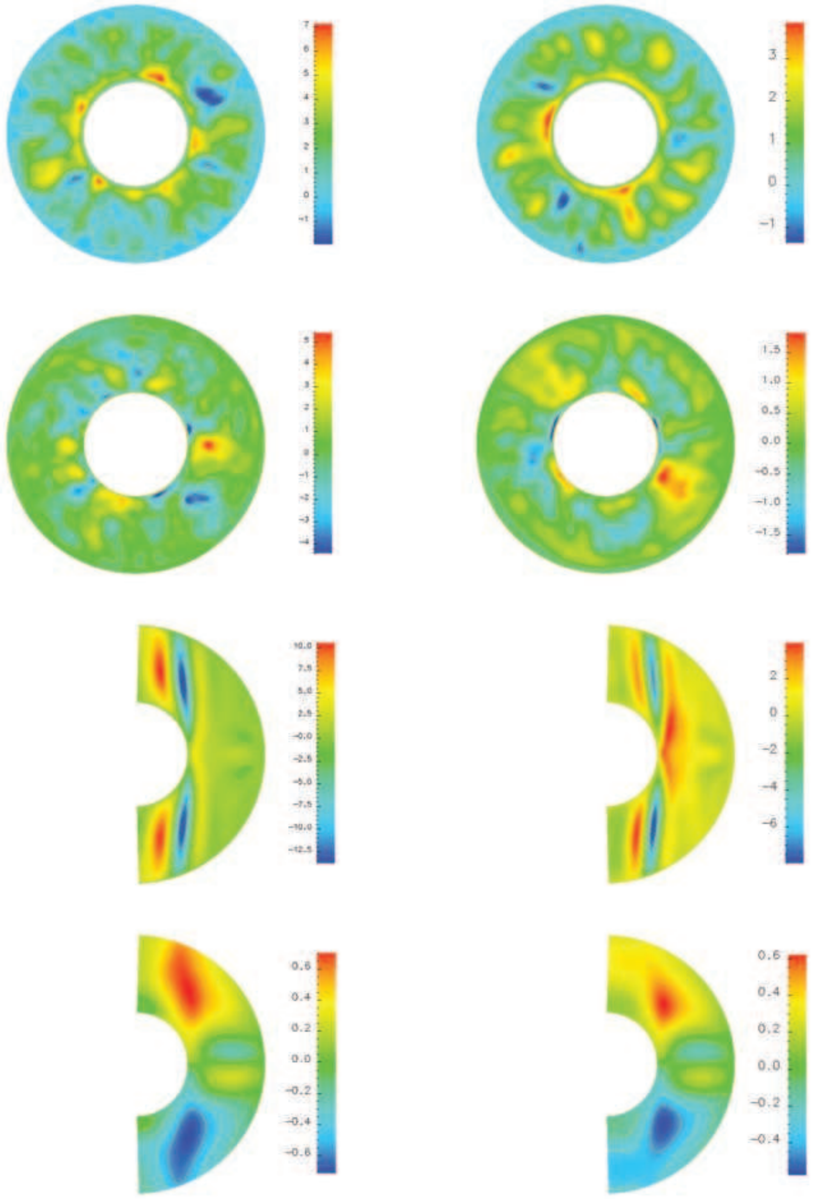

Figure 3. From top to bottom: u_r and u_ϕ in the equatorial plane, u_r and B_r in the meridional plane for models C1-1 (left) and C3-1 (right). Meridional sections are taken at $\phi = \pi$, where $\phi = 0$ is at the right-hand edge of the equatorial projections.

model C1-1 do not result in stronger B_r compared to model C3-1 although the columns of B_r do penetrate closer to the outer boundary in the former Case. The equatorially antisymmetric nature of B_r in both models is reflected in the values of $ME_{\mathcal{S}}/ME$ in Table 4.

Despite differences in the internal structure of the magnetic and velocity fields for models C1-1 and C3-1 the generated magnetic fields at the outer boundary (OB) are very similar:

they are stable and axially dipolar in the time-average (magnetic energy spectra peak at $l = 1$ and $m = 0$ in Figure 2). Averaging the models over 10 magnetic diffusion times has removed any longitudinal structure and left only the field component with the longest time-constant, the axial dipole. Longitudinal variations are also absent in the flow patterns near the OB in both Cases, which may explain why the different flow structures that persist deep inside the shell are not seen at the surface.

Projections of the solutions for $ERa = 50$ are shown in Figure 3 averaged over 2 magnetic diffusion times. Equatorial flow patterns are more complex than at lower ERa as can be appreciated from the flatter kinetic energy spectra in Figure 2 for the Cx-3 models than the Cx-1 models. For Case 1 the equatorial pattern of u_r is dominated by two patches of high velocity (as was the case for $ERa = 10$), the amplitude of which is much greater than the maximum velocity in either Case 2 or 3. In Case 2 u_r is negative near the OB where the superadiabatic heat-flux is very small and mixing is achieved mainly by the compositional sink. In Case 3 the pattern of u_r is very different to model C3-1 in Figure 3; the simple pattern identified at $ERa = 10$ has been replaced with small-scale flow structures than span the shell in the equatorial plane, which likely results from the dominance of uniform internal heating in the buoyancy profile. The pattern of u_ϕ for model C1-3 is dominated by small-scales as for $ERa = 10$; by comparison the equatorial projections of u_ϕ for Cases 2 and 3 are large-scale.

Patterns of $\mathbf{u}$ and $\mathbf{B}$ in meridional planes are similar to those at $ERa = 10$ and are omitted in favour of plots of B_r in the equatorial plane. For model C1-3 negative B_r is mostly confined to narrow structures emanating from the IB, while B_r is positive throughout the rest of the shell. Positive B_r dominates in Case 2 save for one large negative patch near the mid-radius of the shell. In Case 3 there are essentially two concentric rings of B_r, one negative deep inside the shell and one positive at larger radii. As with the $ERa = 10$ models, differences in the internal structure of the flow and field are much greater than differences observable at the OB. Projections of B_r at the OB in Figure 4 show that both models C1-3 and C3-3 have weak flux near the poles and reversed flux in equatorial regions; neither of these features are present for model C2-3. Differences between Cases 1 and 3 are observed just outside the tangent cylinder: in model C1-3 there is a large patch of magnetic flux in each hemisphere, while in model C3-3 there are several smaller patches of flux that are smeared out due to the averaging. These variations may reflect differences in the internal magnetic field configuration near the IB or may be due to to the choice of averaging time; this has not been investigated, but it should be noted that 2 diffusion times is much longer than the 10kyr time period spanned by current global time-dependent geomagnetic field models (Korte & Constable, 2006).

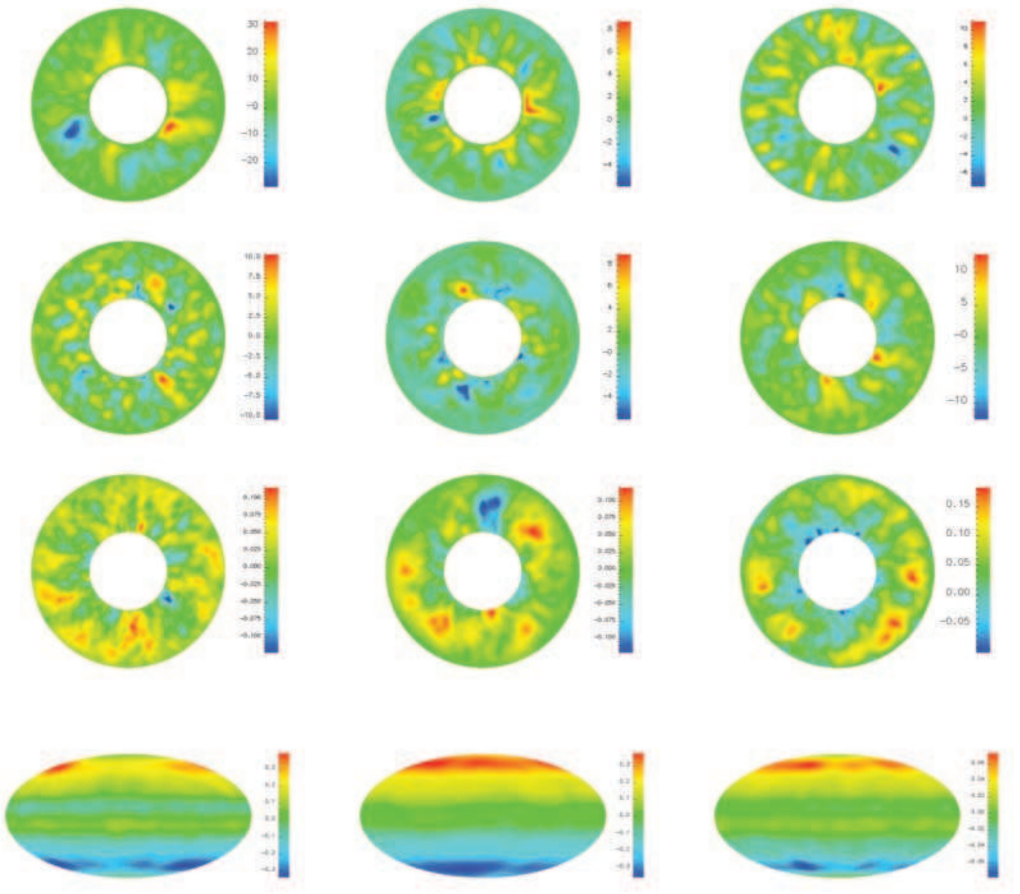

Figure 4. From top to bottom: u_r, u_ϕ and B_r in the equatorial plane, B_r at the OB truncated at harmonic degree 12 for models C1-3 (left), C2-3 (middle) and C3-3 (right). Meridional sections are taken at $\phi = \pi$. Models are averaged for 2 diffusion times.

Figure 5 shows B_r at the OB for models with $ERa = 200$. There is a significant increase in the spatial complexity of the fields compared to lower ERa models, reflected in the flatter magnetic energy spectra (Figure 2), which is partly because the models are driven harder and partly because of the shorter averaging time. There are significant differences between the surface fields for the different Cases. For Case 1 the unfiltered field contains reversed flux near the equator and a strong dipole component of reversed polarity; filtering the field to degree 12 reveals two or three patches of magnetic flux in each hemisphere located at high latitudes that are reminiscent of those identified in historical (Jackson et al., 2000) and paleomagnetic (Korte et al., 2009) geomagnetic field models. For Case 2 the axial dipole is pronounced, reflecting the weaker radial buoyancy force near the OB; the filtered and unfiltered fields are very similar, indicating that most of the energy is contained in large scales (Figure 2). The

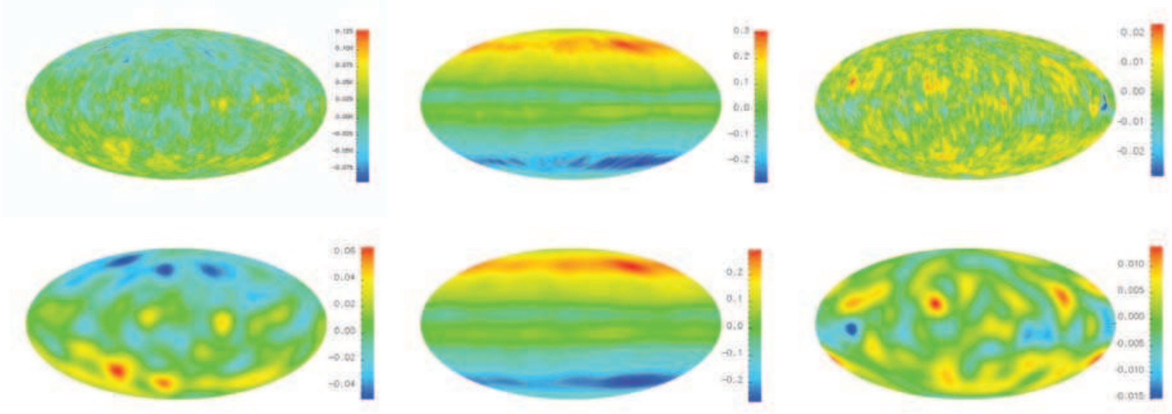

Figure 5. B_r at the OB unfiltered (top) and truncated at spherical harmonic degree 12 (bottom) for models C1-5 (left), C2-5 (middle) and C3-5 (right).

field for Case 3 is non-axisymmetric and nondipolar; the unfiltered and filtered fields look very different, indicating that significant energy is contained in small scales (Figure 2). In Cases 1 and 3 the surface field strength has decreased compare to the $ERa = 50$ solutions (Figure 4), while for Case 2 the field strength has increased; however, the total magnetic energy for Cases 1 and 2 has increased while for Case 3 it has decreased (see Figure 2). This result agrees with the scaling of Olson & Christensen (2006) and may reflect the high degree of internal heating in Case 3.

Time-averaged properties of solutions with $ERa = 200$ are shown in Figure 6. Equatorial sections of u_r display similar characteristics to those with $ERa = 50$: Cases 1 and 2 are dominated by localised patches of high velocity at depth where the buoyancy force is strongest, while the flow pattern for Case 3 consists of small-scales that span the equatorial plane, which likely reflects the high degree of internal heating. Convection is most vigorous for Case 1 as in previous Cases, but unlike the models with $ERa = 50$ Case 3 has the weakest radial motions when viewed in the equatorial plane. Meridional sections show strong quasi-columnar motion outside the tangent cylinder for all Cases, indicating that rotational effects remain significant even at high ERa; the high values of $KE_{\mathcal{T}}/KE$ and $KE_{\mathcal{S}}/KE$ in Table 4 support this.

Finally we consider the time-dependence of the axial dipole harmonic g_1^0 for solutions with $ERa = 200$ (Figure 7). Model 1-5 reverses occasionally; in stable polarity intervals the dipole coefficient is much greater than in any other Case. Model 2-5 is a stable, non-reversing dynamo with a small value of g_1^0 compared to the other runs; this coefficient still dominates all others. Model 3-5 reverses very regularly and its spatial structure is always dominated by higher multipoles.

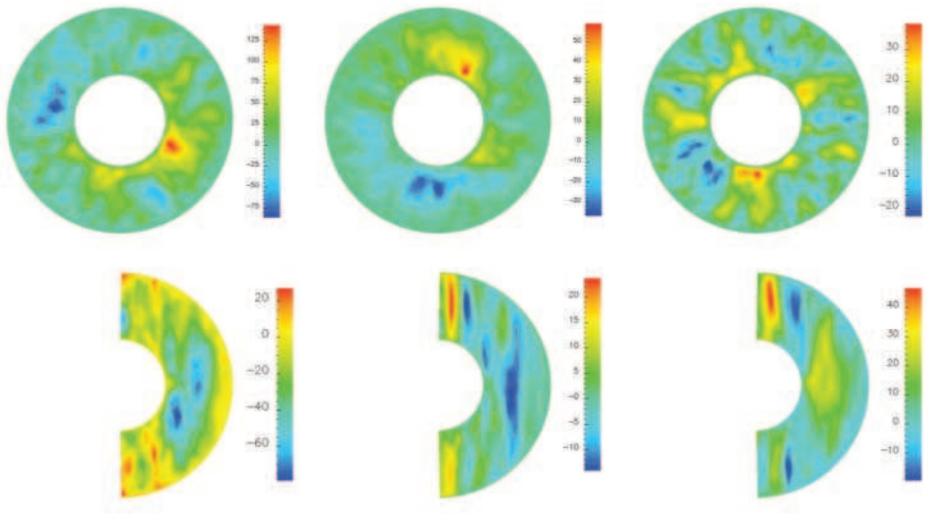

Figure 6. Time-averaged radial velocity in the equatorial (top) and meridional (bottom) planes, for Case 1c (left), Case 2d (middle), and Case 3d (right). Meridional sections are taken at $\pi/2$. Models are averaged over one magnetic diffusion time.

5 SUMMARY AND CONCLUSIONS

We have derived a radial buoyancy profile for Earth's core and shown that, to a good approximation, it corresponds to a combination of bottom heating and uniform heat sinks. The profile combines compositional and thermal buoyancy into a single cotemperature formulation,

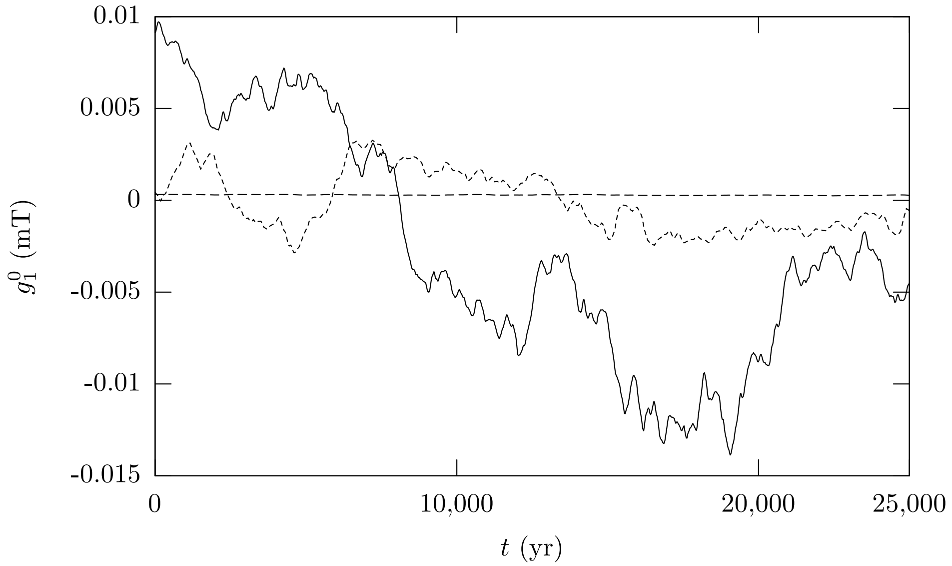

Figure 7. Time-series of the spherical harmonic coefficient g_1^0 (the axial dipole coefficient) for models 1-5, 2-5 and 3-5. The timespan is the final 25,000 years of each run.

allowing comparison of the different buoyancy effects, and can be easily generalised for the case where thermal and compositional diffusivities differ and two diffusion equations are used. The relative importance of the different buoyancy sources depends on quantities determined from seismology and mineral physics with two exceptions: the cooling rate at the core mantle boundary and the local rate of radiogenic heat production. These parameters are constrained using core energetics calculations; varying them results in a suite of quite distinct buoyancy profiles corresponding to different scenarios for core evolution.

The 3 different Cases of core evolution we have analysed in detail span a good range of the scenarios that have been explored in the literature, from rapid cooling and a young inner core, through moderate cooling and neutral stability at the CMB to very slow cooling and sufficient radiogenic heating to provide a primordial inner core. We find that compositional buoyancy is stronger than thermal buoyancy except near the CMB, where compositional convection ceases altogether. The cotemperature gradient is always greatest at the bottom of the outer core because light material and latent heat are released there. In general, bottom heating is always greater than internal heating even if substantial radiogenic heating is present.

We carried out numerical geodynamo simulations for the 3 different core evolution scenarios. The Rayleigh number is defined based on the temperature gradient across the core, which is independent of the core evolution model, and had to be scaled down with the Ekman number in order to retain the magnetogeostrophic balance that pertains in the Earth's core. The 3 core evolution scenarios define the balance of internal and bottom heating. Solutions from the geodynamo simulations are quite different in the 3 Cases; while firm conclusions cannot be drawn from the number of runs we have performed, our results suggest that it may be possible to discriminate between the various core evolution scenarios by exploring their effect on the generated fields. At low Rayleigh number the principle differences are in the flow patterns: significant bottom heating causes patches of high velocity, while dominant internal heating leads to small-scale flow structures with much lower velocity. Significant differences emerge at higher Rayleigh numbers. For rapid cooling the dynamo reverses and the time-averaged field is dominated by large-scale features at high latitudes that are reminiscent of the present geomagnetic field, while for moderate cooling the dynamo is stable and always dominated by the axial dipole. Dominant internal heating produces non-dipolar surface fields with very frequently reversals suggesting this combination of heating is not acceptable for a geodynamo model.

Like the study of Kutzner & Christensen (2000) we find that the internal patterns of the velocity and magnetic fields differ between the various Cases at all Rayleigh numbers we consider. Unlike their study, however, we find that these differences are not observed in the surface field at low Rayleigh numbers, which are stable and dipolar. This feature of our models could result from our prescription of a fixed heat-flux outer boundary condition, which promotes large-scale temperature anomalies near the outer boundary (Aubert et al., 2009; Sakuraba & Roberts, 2009), while Kutzner & Christensen (2000) used a fixed temperature outer boundary condition. At high Rayleigh number we observe different behaviour of reversing dynamos between different core evolution models in agreement with the results of Kutzner & Christensen (2002). Finally, we note that the equations derived in Section 2 provide a consistent means for defining reference states at any point in the past. This represents an alternative method to the scaling analysis undertaken by Aubert et al. (2009) for investigating the paleofield in dynamo models. In particular, prior to inner core formation our equations consistently reduce to a reference state consisting of purely thermal buoyancy.

Our results indicate that geodynamo models are sufficiently sensitive to buoyancy profile to provide valid tests of suitability of core evolution models. Further work is therefore warranted to explore the dependency of the generated magnetic fields on the many parameters that we have not yet varied.

ACKNOWLEDGMENTS

DG was supported by the Miller Institute for Basic Research in Science, University of California, Berkeley. CD was supported by a Green Fellowship at IGPP. We thank two anonymous referees for their comments.

References

Alfè, D., Gillan, M. J., & Price, G. D., 1999a. The melting curve of iron at the pressures of the Earth's core conditions, *Nature*, **401**, 462–464.

Alfè, D., Price, G. D., & Gillan, M. J., 1999b. Oxygen in the Earth's core: a first-principles study, *Phys. Earth Planet. Int.*, **110**, 191–210.

Anufriev, A., Jones, C., & Soward, A., 2005. The Boussinesq and anelastic liquid approximations for convection in Earth's core, *Phys. Earth Planet. Int.*, **152**, 163–190.

Aubert, J., Labrosse, S., & Poitou, C., 2009. Modelling the palaeo-evolution of the geodynamo, *Geophys. J. Int.*, **179**, 1414–1428.

Braginsky, S., 1963. Structure of the F layer and reasons for convection in the Earth's core, *Sov. Phys. Dokl.*, **149**, 8–10.

Braginsky, S. & Roberts, P., 1995. Equations governing convection in Earth's core and the geodynamo, *Geophys. Astrophys. Fluid Dyn.*, **79**, 1–97.

Buffett, B., Huppert, H., Lister, J., & Woods, A., 1996. On the thermal evolution of the Earth's core, *J. Geophys. Res.*, **101**, 7989–8006.

Busse, F., 1970. Thermal instabilities in rapidly rotating systems, *J. Fluid Mech.*, **44**, 441–460.

Busse, F., Grote, E., & Simitev, R., 2003. Convection in rotating spherical shells and its dynamo action, in *Earth's core and lower mantle*, pp. 130–152, Contributions from the SEDI 2000, The 7th Symposium.

Chandrasekhar, S., 1961. *Hydrodynamic and Hydromagnetic Stability*, International Series of Monographs on Physics, Dover.

Christensen, U. & Aubert, J., 2006. Scaling properties of convection-driven dynamos in rotating spherical shells and application to planetary magnetic fields, *Geophys. J. Int.*, **166**, 97–114.

Christensen, U., Olson, P., & Glatzmaier, G., 1999. Numerical modelling of the geodynamo: a systematic parameter study, *Geophys. J. Int.*, **138**, 393–409.

Christensen, U., Aubert, J., Cardin, P., Dormy, E., Gibbons, S., Glatzmaier, G., Grote, E., Honkura, Y., Jones, C. Kono, M., Matsushima, M., Sakuraba, A., Takahashi, F., Tilgner, A., Wicht, J., & Zhang, K., 2001. A numerical dynamo benchmark, *Phys. Earth Planet. Int.*, **128**, 25–34.

Dormy, E., Soward, S., Jones, C., Jault, D., & Cardin, P., 2004. The onset of thermal convection in rotating spherical shells, *J. Fluid Mech.*, **501**, 43–70.

Driscoll, P. & Olson, P., 2009. Polarity reversals in geodynamo models with core evolution, *Earth Planet. Sci. Lett.*, **282**, 24–33.

Glatzmaier, G. & Roberts, P., 1996. An anelastic evolutionary geodynamo simulation driven by compositional and thermal convection, *Physica D*, **97**, 81–94.

Grote, E., Busse, F., & Tilgner, A., 1998. Regular and chaotic spherical dynamos, *Phys. Earth Planet. Int.*, **117**, 259–272.

Gubbins, D., 2001. The Rayleigh number for convection in the Earth's core, *Phys. Earth Planet. Int.*, **128**, 3–12.

Gubbins, D., Masters, T., & Jacobs, J., 1979. Thermal evolution of the Earth's core, *Geophys. J. R. Astr. Soc.*, **59**, 57–99.

Gubbins, D., Alfe, D., Masters, G., Price, G., & Gillan, M., 2004. Gross thermodynamics of two-component core convection, *Geophys. J. Int.*, **157**, 1407–1414.

Heimpel, M., Aurnou, J., Al-Shamali, F., & Gomez Perez, N., 2005. A numerical study of dynamo action as a function of spherical shell geometry, *Earth Planet. Sci. Lett.*, **236**, 542–557.

Hewitt, J., McKenzie, D. P., & Weiss, N. O., 1975. Dissipative heating in convective flows, *J. Fluid Mech.*, **68**, 721–738.

Hori, K., Wicht, J., & Christensen, U., 2010. The effect of thermal boundary conditions on dynamos driven by internal heating, *Phys. Earth Planet. Int.*, **182**, 85–97.

Jackson, A., Jonker, A., & Walker, M., 2000. Four centuries of geomagnetic secular variation from historical records, *Phil. Trans. R. Soc. Lond. A*, **358**, 957–990.

Jacobs, J., 1953. The Earth's inner core, *Nature*, **172**, 297–300.

Jones, C., 2000. Convection-driven geodynamo models, *Phil. Trans. R. Soc. Lond. A*, **358**, 873–897.

Jones, C., 2007. Thermal and compositional convection in the outer core, in *Treatise on Geophysics Vol. 8, Ch.5*, pp. 133–185, ed. Schubert, G., Elsevier, Amsterdam.

Kono, M. & Roberts, P., 2001. Definition of the rayleigh number for geodynamo simulation, *Phys. Earth Planet. Int.*, **128**, 13–24.

Korte, M. & Constable, C., 2006. Centennial to millennial geomagnetic secular variation, *GJI*, **167**, 43–52.

Korte, M., Donadini, F., & Constable, C., 2009. Geomagnetic field for 0–3ka: 2. A new series of time-varying global models, *Geochem. Geophys. Geosys*, **10**, 1–24.

Kutzner, C. & Christensen, U., 2000. Effects of driving mechanisms in geodynamo simulations, *Geophysics Research Letters*, **27**, 29–32.

Kutzner, C. & Christensen, U., 2002. From stable dipolar towards reversing numerical dynamos, *Phys. Earth Planet. Int.*, **131**, 29–45.

Labrosse, S., Poirier, J.-P., & Le Moeul, J.-L., 1997. On cooling of the Earth's core, *Phys. Earth Planet. Int.*, **99**, 1–17.

Manglik, A., Wicht, J., & Christensen, U., 2010. A dynamo model with double diffusive convection for Mercury's core, *Earth Planet. Sci. Lett.*, **209**, 619–628.

Mihaljan, J. M., 1962. A rigorous exposition of the Boussinessq approximations applicable to a thin layer of fluid, *Astrophys. J.*, **136**, 1126–1133.

Nimmo, F., 2007. Thermal and compositional evolution of the core, in *Treatise on Geophysics, Vol. 8*, pp. 217–241, ed. Schubert, G., Elsevier, Amsterdam.

Nimmo, F., Price, G., Brodholt, J., & Gubbins, D., 2004. The influence of potassium on core and geodynamo evolution, *Geophys. J. Int.*, **156**, 363–376.

Ogden, D., Glatzmaier, G., & Coe, R., 2006. The effects of different parameter regimes in geodynamo simulations, *Geophys. Astrophys. Fluid Dyn.*, **100**, 107–120.

Olson, P., 2007. Gravitational dynamos and the low-frequency geomagnetic secular variation, *Proc. Natl. Acad. Sci.*, **104**, 20159–20166.

Olson, P. & Christensen, U., 2006. Dipole moment scaling for convection-driven planetary dynamos, *Earth Planet. Sci. Lett.*, **250**, 561–571.

Olson, P., Christensen, U., & Glatzmaier, G., 1999. Numerical modeling of the geodynamo: Mechanisms of field generation and equilibration, *J. Geophys. Res.*, **104**, 10,383–10,404.

Olson, P., Coe, R., Driscoll, P., Glatzmaier, G., & Roberts, P., 2010. Geodynamo reversal frequency and heterogeneous core-mantle boundary heat flow, *Phys. Earth Planet. Int.*, **180**, 66–79.

Olson, P., Glatzmaier, G., & Coe, R., 2011. Complex polarity reversals in a geodynamo model, *Earth Planet. Sci. Lett.*, **304**, 168–179.

Rotvig, J., 2009. An investigation of reversing numerical dynamos driven by either differential or volumetric heating, *Phys. Earth Planet. Int.*, **176**, 69–82.

Sakuraba, A. & Roberts, P., 2009. Generation of a strong magnetic field using uniform heat flux at the surface of the core, *Nature Geosci.*, **2**, 802–805.

Spiegel, E. & Veronis, G., 1960. On the Boussinesq approximation for a compressible fluid, *Astrophys. J.*, **131**, 442–447.

Sreenivasan, B. & Gubbins, D., 2008. Dynamos with weakly convecting outer layers: implications for core-mantle boundary interaction, *Geophys. Astrophys. Fluid Dyn.*, **102**, 395–407.

Sreenivasan, B. & Jones, C., 2006. Azimuthal winds, convection and dynamo action in the polar regions of planetary cores, *Geophys. Astrophys. Fluid Dyn.*, **100**, 319–339.

Verhoogen, J., 1961. Heat balance of the Earth's core, *Geophys. J. R. Astr. Soc.*, **4**, 276–281.

Willis, A., Sreenivasan, B., & Gubbins, D., 2007. Thermal core-mantle interaction: exploring regimes for 'locked' dynamo action, *Phys. Earth Planet. Int.*, **165**, 83–92.

Zhang, K., 1992. Spiralling columnar convection in rapidly rotating spherical fluid shells, *J. Fluid Mech.*, **236**, 535–556.

Zhang, K. & Schubert, G., 2000. Magnetohydrodynamics in rapidly rotating spherical systems, *Annu. Rev. Fluid Mech.*, **32**, 409–443.